

Mixed Electron–Proton Conductors Enable Spatial Separation of Bond Activation and Charge Transfer in Electrocatalysis

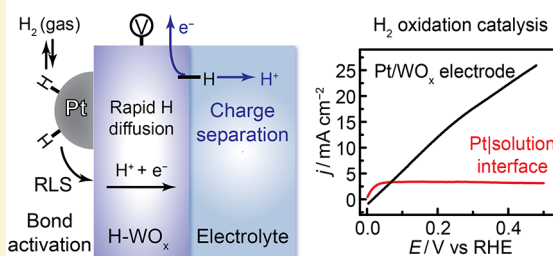
Bing Yan,¹ Ryan P. Bisbey, Alexander Alabugin,² and Yogesh Surendranath^{1*}

Department of Chemistry, Massachusetts Institute of Technology, Cambridge, Massachusetts 02139, United States

Supporting Information

ABSTRACT: Electrochemical energy conversion requires electrodes that can simultaneously facilitate substrate bond activation and electron–proton charge transfer. Traditional electrodes co-localize both functions to a single solid/liquid interface even though each process is typically favored in a disparate reaction environment. Herein, we establish a strategy for spatially separating bond activation and charge transfer by exploiting mixed electron–proton conduction (MEPC) in an oxide membrane. Specifically, we interpose a MEPC WO_x membrane between a Pt catalyst and aqueous electrolyte and show that this composite electrode is active for the hydrogen oxidation reaction (HOR). Consistent with H_2 activation occurring at the gas/solid interface, the composite electrode displays HOR current densities over 8-fold larger than the diffusion-limited rate of HOR catalysis at a singular Pt/solution interface. The segregation of bond activation and charge separation steps also confers excellent tolerance to poisons and impurities introduced to the electrolyte. Mechanistic studies establish that H_2 activation at the Pt/gas interface is coupled to the electron–proton charge separation at the WO_x /solution interface via rapid H-diffusion in the bulk of the WO_x . Consequently, the rate of HOR is principally controlled by the rate of H-spillover at the Pt/ WO_x boundary. Our results establish MEPC membrane electrodes as a platform for spatially separating the critical bond activation and charge transfer steps of electrocatalysis.

Mixed Electron–Proton Conductor Electrocatalysis



INTRODUCTION

Electrochemical energy conversion relies on the efficient transfer of electron–proton or H-atom equivalents to and from small molecule substrates such as water,^{1–5} H_2 ,^{6–9} O_2 ,^{10–13} and CO_2 .^{14–17} Irrespective of the small molecules of interest, the electrochemical interface must carry out two critical functions. Taking the oxidation of H_2 as an example, the interface must facilitate (1) the activation of the substrate to generate surface-bound H-atom equivalents (Figure 1, black), and (2) the separation of these adsorbed H-atom equivalents into electrons and protons (Figure 1, blue). Although the mechanistic details may be far more complex for other substrates, a similar sequence of bond activation and charge transfer steps will be involved in any electrocatalytic reaction. Traditionally, a singular solid/liquid interface carries out both functions (Figure 1a), but this is rarely ideal because (1) and (2) are often each favored in disparate reaction environments. For example, while aqueous electrolytes provide for rapid proton conductivity and therefore facilitate electron–proton charge separation (2), they display poor solubility for gaseous substrates¹⁸ which in turn limits the rate of substrate bond activation (1). While gas-diffusion electrodes overcome the solubility issues by forming a gas/liquid/solid triphase boundary, the two functions (1 and 2) remain co-localized to the same interface preventing independent optimization of each.¹⁹ Likewise, competitive adsorption of solvent and/or buffering ions (X in Figure 1a) is known to impede substrate

activation at catalyst active sites (1),^{20–23} but can be essential for promoting electron–proton transfer reactions (2).^{24–29} Furthermore, adventitious electrolyte impurities and crossover species which are commonplace in electrochemical devices can interfere with substrate activation (1),^{30–32} but often do not interfere with the electron–proton transfer (2). Clearly, the development of next-generation energy conversion technologies would benefit from new strategies that address the incompatibilities of functions (1) and (2).

In principle, the two functions of substrate bond activation (1) and electron–proton transfer (2) can be separated spatially and chemically by interposing a membrane between the catalyst and the electrolyte. Unlike the traditional ion conducting membranes used in electrochemical devices, this concept requires a membrane that selectively transports H-atom equivalents while rejecting the transfer of gas, solvent, and ions between catalyst and electrolyte. The membrane must also be catalytically inert, excluding consideration of Pd-based membranes^{33–36} that can carry out catalysis at the electrolyte junction. These dual requirements favor the use of nonporous condensed solid oxides. Although ion conductivity in solid oxides is typically sluggish for electronic insulators,³⁷ many oxides are known to rapidly intercalate electron–proton pairs upon polarization^{38–41} or via spillover from active cata-

Received: March 27, 2019

Published: June 2, 2019

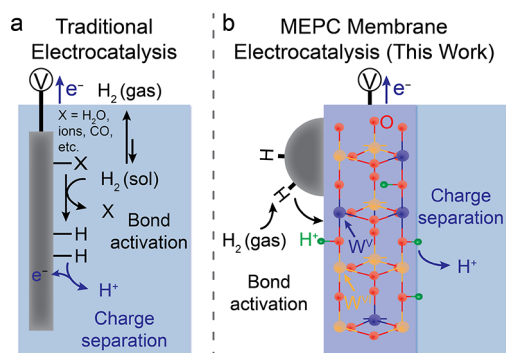


Figure 1. Schematic representations of HOR catalysis by (a) a traditional singular solid/liquid electrochemical interface and (b) WO_x MEPC membrane interface. (a) The overall HOR process involves gaseous H_2 dissolution, charge displacement of surface-adsorbed species X (X can be the solvent H_2O , electrolyte ions, dissolved gases such as CO , etc.), bond activation of the dissolved H_2 to form surface-adsorbed H atoms, and electron-proton charge separation. (b) H_2 bond activation takes place at the gas/solid interface and electron-proton charge separation occurs at the solid/electrolyte interface. The color scheme of the WO_x ball-and-stick model of (b): red, O; orange, W(VI); blue, W(V); and green, H.

lysts.^{42,43} By matching the proton intercalation potential to that of the terminal electrocatalytic reaction, we envision that the H-atom equivalents within mixed electron-proton conductors (MEPCs) could drive catalytic reactions at gas/solid interfaces, thereby spatially separating the functions of bond activation and electron-proton charge separation for the first time.

Herein, we establish the feasibility of MEPC membrane mediated electrocatalysis by constructing a composite anode consisting of a MEPC membrane interposed between a Pt catalyst and aqueous electrolyte (Figure 1b). For this proof-of-concept study, we prepared an amorphous tungsten oxide (WO_x) membrane that has an H intercalation potential matched to that of the H_2/H^+ couple.⁴⁴ We show that rapid

H-conduction in WO_x drives overall hydrogen oxidation reaction (HOR) catalysis with H_2 activation and H-spillover occurring at the gas/solid interface and electron-proton transfer occurring at the WO_x /electrolyte interface.

Preparation and Characterization of Pt/ WO_x Composite Membranes. Pt/ WO_x composite films were prepared on porous polycarbonate supports using the procedure depicted in Figure 2a (see the Supporting Information, SI, for full fabrication details). Briefly, we employed a polycarbonate membrane with 200 nm pores as the inert mechanical support for the Pt/ WO_x composite films. RF magnetron sputtering of W in the presence of O_2 was first used to deposit a dense layer of WO_x on the polycarbonate support (Figure 2b).^{45–47} Subsequently, Pt was deposited on WO_x via DC magnetron sputtering. SEM images indicate the formation of a smooth continuous WO_x film, free of large pinholes or cracks (Figures 2c and S1). SEM/EDS analysis confirms the presence of Pt (Figure S2) and reveals a W:O ratio of 1:2.86, consistent with an oxygen-deficient WO_3 layer. This WO_x layer is amorphous as judged by the absence of peaks in the XRD (Figure S3) of as-prepared films. Survey XPS spectra of the as-prepared Pt/ WO_x films show peaks corresponding to Pt, W, O, and adventitious C (Figure S4). High-resolution scans of the W region reveal two sets of W $4f_{7/2}$ and $4f_{5/2}$ peaks (Figure 2e). The binding energies of the $4f_{7/2}$ peaks are 36.2 and 33.1 eV and correspond to W(VI) and W(V), respectively.⁴⁸ Peak ratios extracted from curve fitting yield an estimated VI:V ratio of 3:1, in line with the 2.6:1 ratio calculated from the bulk W:O stoichiometry determined by SEM/EDS. The Pt $4f_{7/2}$ peak is observed at a binding energy of 71.5 eV (Figure 2f), indicative of metallic Pt.⁴⁹ To gain insight into the Pt morphology, we prepared a Pt/ WO_x film on a TEM grid with a thin ~ 40 nm WO_x layer. TEM images reveal discrete, crystalline, ~ 5 nm islands dispersed uniformly on the WO_x layer (Figure 2d). STEM-EDS point analysis indicates the presence of Pt at image regions containing lattice fringes and the absence of Pt at amorphous regions on the surface (Figure S5). Moreover, fast Fourier transform reveals spots for the

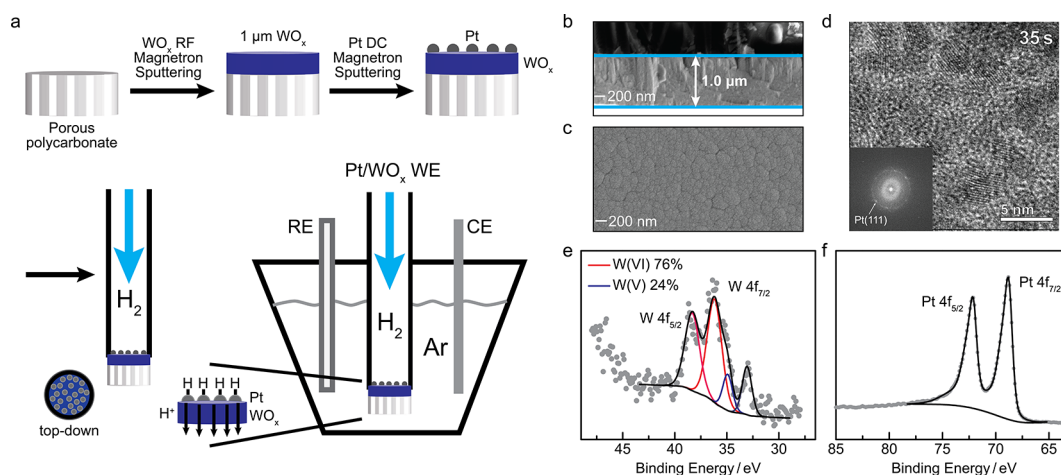


Figure 2. Fabrication and characterizations of the Pt/ WO_x composite electrode. (a) Schematic representation of the fabrication of the Pt/ WO_x composite electrode. In the top-down view of the composite electrode, the black periphery illustrates the position of the Ag paint electrical contact. (b) Cross-section SEM image of the magnetron sputter deposited Pt/ WO_x film, supported on a porous polycarbonate membrane. (c) Top-down SEM image of the Pt/ WO_x film. (d) TEM image of Pt islands supported on ~ 40 nm WO_x films which were deposited on a Cu/lacey carbon TEM grid. (e) XPS spectrum and peak-fitting of W $4f$ region of the as-prepared Pt/ WO_x films. The gray dots are the experimental data. The red and blue lines represent the fitted W $4f_{7/2}$ and $4f_{5/2}$ peaks for W(VI) and W(V), respectively. The black lines depict the fitting envelope and the background. (f) XPS spectrum of Pt $4f$ region of the as-prepared Pt/ WO_x films.

observed fringes consistent with the spacings for Pt(111) (Figure 2d, inset). The results support the assignment of these islands as crystalline Pt nanoparticles. TEM images reveal no lattice fringes for the WO_x layer (Figure 2d), consistent with the absence of peaks in the XRD (Figure S3). Together, the above data indicate that this preparation method generates a Pt/ WO_x composite film consisting of ~ 5 nm diameter Pt islands uniformly distributed on a smooth, continuous, amorphous layer of oxygen-deficient WO_x .

The Pt/ WO_x composite film prepared by the above procedure was fashioned into a membrane electrode assembly by sealing the sample onto one end of a carbon fiber tube with silver paint adhesive. The Pt-containing side of the WO_x was oriented toward the inside of the carbon tube and the silver paint provided both a low-resistivity contact to the WO_x and a gastight seal between the Pt side and the electrolyte (Figure 2a). The entire assembly was then further sealed with epoxy to prevent silver leaching into the solution. This carbon fiber tube served as the working electrode with the H_2 reactant flowed to the inside of the tube (Figure 2a). The absence of gas bubbles on the solution-facing side of the composite anode provided a first indication that this fabrication procedure generates a gastight seal. This observation is complemented with CO poisoning experiments and Cu tracer studies, detailed below, that provide direct evidence for rigorous exclusion of gas and liquid exchange between gas-facing and solution-facing sides of the composite anode (SI).

Pt/ WO_x MEPC Membrane Electrode Catalyzes HOR.

To study the HOR activity of the Pt/ WO_x composite electrode, we supplied 1 atm of H_2 to the Pt side of the composite film and exposed the WO_x side to 0.1 M HClO_4 , pH 1.0, electrolyte. Cyclic voltammetry (CV) was performed from 0.00 to 0.52 V (all potentials are reported versus the reversible hydrogen electrode (RHE) unless otherwise noted) at a 50 mV s^{-1} scan rate. The initial CV scan displays a roughly linear rise in current from 0 to 18 mA cm^{-2} as the potential was swept between 0.00 to 0.52 V (Figure S6). Subsequent cycling over the same potential range led to the steady rise in the magnitude of the current before reaching a maximum stable value shown in Figure 3a, black. The resulting voltammetric response exhibits a linear rise in current from 0 to 25 mA cm^{-2} over the potential range examined. Substitution of the H_2 flow for N_2 led to a rapid decay of the current, eventually reaching a background level shown in Figure 3a, red. The background trace still displays current attributed to the stoichiometric electrochemical intercalation/deintercalation of H into/out of WO_x , but the dramatic current enhancement observed when H_2 is flowing is entirely absent. These observations, taken together, indicate that the Pt/ WO_x composite electrode is able to catalyze the overall H_2 oxidation reaction. Notably, in the presence of H_2 , the current density reaches a value in excess of 25 mA cm^{-2} , which is 8-fold higher than the diffusion-limited rate of HOR catalysis if the Pt catalysts are directly exposed to the electrolyte (Figure 3a, blue dash). This dramatic current enhancement indicates that H_2 activation is occurring at the gas/solid interface rather than in solution.

The HOR activity is maintained at a steady state. Chronoamperometry (CA) traces collected at a variety of potentials reveal that the HOR currents reached steady state rapidly (Figure S7), indicating that the rate of H_2 activation and H-spillover at the gas/solid junction is balanced by the rate of electrochemical electron–proton charge separation at the

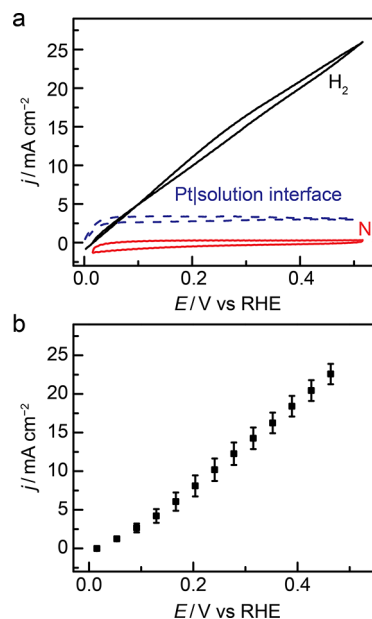


Figure 3. (a) Cyclic voltammogram (CV) of the Pt/ WO_x composite electrode with N_2 (red) and H_2 (black) supplied to the working electrode. The CV of HOR catalysis at a singular Pt/solution interface is also plotted for comparison (blue dash). (b) Steady-state HOR current densities recorded in Ar-saturated 0.1 M HClO_4 , with H_2 supplied to the gas/solid interface of the working electrode. The error bars represent the standard error of the mean calculated from three independent film preparations.

WO_x /solution interface. The steady-state current densities are plotted versus potential from 0.00 to 0.48 V in 40 mV increments (Figure 3b) and are similar in magnitude to the values observed in the CV data. These observations indicate that the Pt/ WO_x composite electrode is able to mediate persistent HOR catalysis, driven by the applied potential.

Interestingly, both the CV and CA reveal two characteristic features. First, they do not display the transport-limited plateau current that is common for HOR at the well-known Pt/solution interface. This lack of a potential-invariant current plateau suggests that reactant diffusion is not limiting and H-diffusion through the WO_x membrane is rapid (see below). Second, the CV and CA data reveal a roughly linear relationship between applied potential and measured HOR current. This linear I – V behavior is in stark contrast to the exponential I – V relationship predicted by the Butler–Volmer equation for an activation-controlled catalytic reaction. This discrepancy can be explained, in part, by recognizing that, for the Pt/ WO_x composite electrode, the applied potential only directly increases the driving force of electron–proton charge separation at the WO_x /solution junction, but only imparts an indirect effect on the rate of H-diffusion through the WO_x and the rate of H_2 activation and H-spillover at the Pt/ WO_x interface. All of these processes are analyzed in greater detail below.

MEPC Membranes Confer Immunity to Electrolyte Impurities. The Pt/ WO_x composite electrode displays high tolerance to impurities and poisons in the electrolyte. For fuel cell applications, O_2 crossover from the cathode is a pernicious problem that leads to efficiency losses.^{50,51} Indeed, for a Pt electrode in direct contact with the electrolyte, the introduction of a 1:1 mixture of O_2 and H_2 , leads to a negligible overall current due to the superimposition of the

anodic HOR current and the cathodic ORR current (Figure S8a). In contrast, for the Pt/WO_x composite electrode, the introduction of 1 atm of O₂ to the electrolyte side leads to unchanged steady-state HOR currents (Figure 4, red) relative

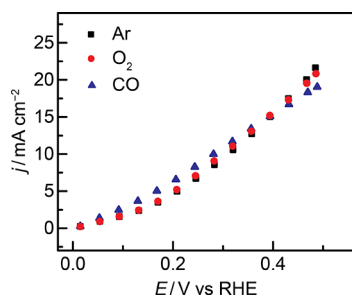


Figure 4. Steady-state HOR current density of the Pt/WO_x composite electrode in the presence of gaseous impurities dissolved in the electrolyte. The data were collected in Ar- (black ■), O₂- (red ●), and CO-saturated (blue ▲) 0.1 M HClO₄.

to those collected in the absence of O₂ (Figure 4, black). While these results suggest that there is minimal gas crossover to the Pt side, we further evaluated the impermeability of the WO_x layer by introducing CO to the solution. As CO impurities are known to readily poison Pt surfaces,^{52–54} this gas provides a stringent test for pinhole defects in the film. We find that, for a Pt electrode in direct contact with the electrolyte, the introduction of CO leads to complete elimination of HOR catalysis (Figure S8b). In stark contrast, for the Pt/WO_x composite electrode, the introduction of 1 atm of CO to the electrolyte side leads to steady-state HOR currents (Figure 4, blue) that are again unchanged relative to those collected in the absence of CO (Figure 4, black). These results establish, (1) that the dense WO_x membrane is pinhole free, effectively rejecting gaseous electrolyte impurities from reaching the Pt catalyst surface, and (2) that the WO_x/electrolyte interface itself is catalytically inert and tolerant of poisoning gases.

In addition to gaseous impurities, the Pt/WO_x composite electrode also displays excellent tolerance to impurity ions in the electrolyte. To provide a direct comparison, we polarized a Pt electrode in contact with electrolyte at 0.50 V in the presence of H₂. Introduction of 10 mM Cu(ClO₄)₂ led to a rapid and progressive decline of HOR activity (Figure S9a). This potential corresponds to the underpotential deposition (UPD) region for Cu on Pt⁵⁵, so we attribute this decline in HOR activity to the formation of a poisoning UPD Cu adlayer on the Pt surface. In contrast, for the Pt/WO_x composite electrode polarized at the same potential, the introduction of the same concentration of Cu(ClO₄)₂ into the electrolyte led to no diminishment of the HOR current (Figure S9b). The absence of Cu poisoning for the Pt/WO_x electrode is corroborated by XPS and ICP-MS. Following polarization of the Pt/WO_x in the presence of 10 mM Cu(ClO₄)₂ in the electrolyte, we examined the composition of the Pt side by XPS (Figure S9c) and ICP-MS (Table S1) which evinced the complete absence of any Cu species. These results reiterate that (1) the dense WO_x membrane is pinhole free, effectively rejecting electrolyte from reaching the Pt catalyst surface and (2) the WO_x/electrolyte interface is itself tolerant to ionic electrolyte impurities.

Mechanistic Studies of MEPC Membrane-Mediated HOR. As noted earlier, the voltammetric profile of the Pt/WO_x

composite electrode does not match that expected for activation-controlled HOR catalysis, nor does it display the characteristic plateau current expected for transport-limited HOR. To further understand the factors that contribute to the rate of HOR catalysis, we systematically varied the structure of the Pt/WO_x composite electrode.

Overall HOR catalysis requires electron–proton transport through the thick WO_x membrane from the gas/solid interface to the oxide/electrolyte boundary. To investigate whether electron–proton transport in WO_x is limiting the HOR current, we prepared WO_x membranes of 0.8, 1.0, and 1.4 μm thickness (Figures 2b and S10) by varying the sputtering time duration from 2.5 to 4 h. The low end of the WO_x membrane thickness was limited by the requirement for a pinhole free, condensed film structure; the high end of the WO_x membrane thickness was limited by the slow deposition rate of magnetron sputtering. For each film thickness, the WO_x surface morphology remains unchanged (Figure S11) and the Pt deposition was conducted simultaneously for all samples to preserve a similar Pt/WO_x boundary density across the film thicknesses examined. Each film performed HOR catalysis and the steady-state HOR currents were the same within error for all of the films across the entire 0.00 to 0.48 V range examined (Figure S12). This remarkable invariance of the HOR rate is shown in Figure 5a for polarization at 0.48 V. Despite a near

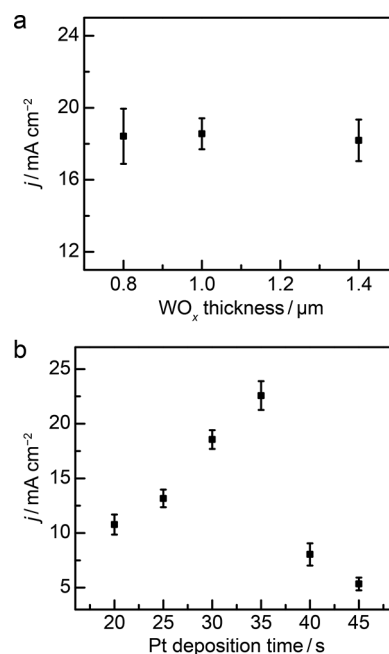


Figure 5. (a) Steady-state HOR current density at 0.48 V versus WO_x membrane thickness. The time duration of Pt sputtering was 30 s for all samples. (b) Steady-state HOR current density at 0.48 V versus the time duration of Pt sputtering. The time duration of WO_x sputtering was 3 h for all samples. The error bars represent the standard error of the mean calculated from three independent film preparations.

doubling of the film thickness, the steady-state HOR current densities remain the same within error at ~18 mA cm^{−2}. These results indicate that electron–proton transport within the WO_x membrane is not limiting the rate of HOR electrocatalysis across the film thickness range examined here. While electron–proton motion has been postulated to be rapid in WO_x,^{42,56–64} our findings provide the first unambiguous confirmation of this

phenomenon and highlight the power of correlated electron motion in promoting solid-state ion transport at low temperatures. We acknowledge that our studies are practically limited by the range of WO_x membrane thicknesses examined, and we expect that the H-diffusion would start to limit the overall rate of HOR catalysis for dramatically thicker WO_x membranes.

HOR catalysis by the Pt/WO_x composite electrode is initiated by H_2 activation and H-spillover at the gas/solid ($\text{H}_2/\text{Pt}/\text{WO}_x$) interface. While it is recognized that the dissociative adsorption of H_2 is extremely rapid at Pt surfaces, H-spillover at the Pt/WO_x boundary is known to be significantly slower.^{60,65–69} To examine whether the rate of H-spillover limits the rate of HOR in our configuration, we systematically varied the loading of Pt on the WO_x membrane by varying the time duration of Pt sputter deposition from 20 to 45 s. TEM analysis reveals that, for deposition times ranging from 20 to 35 s, the Pt morphology consists of isolated islands on the WO_x films. Over this series of deposition times, the Pt island density increases but the average diameter of each island remains constant at ~ 5 nm (Figures 2d and S13a–d). For deposition times beyond 40 s, these Pt islands evolve into an interconnected array of Pt with randomly arranged gaps that expose the WO_x membrane. (Figure S13e,f). The observed HOR current densities are strongly correlated with these changes in Pt morphology. With increasing Pt deposition time from 20 to 35 s, we observe a corresponding systematic rise in the HOR current density from 11 to 23 mA cm^{-2} at 0.48 V (Figure 5b). This rise is then followed by a sudden drop in HOR current to 7 and 5 mA cm^{-2} for the 40 and 45 s deposition samples, respectively (Figure 5b). These changes in HOR current density with Pt deposition time are also reflected across the entire 0.00 to 0.48 V range examined here (Figures 3b and S15).

The correlated changes in the HOR current with a variation of the Pt morphology can be rationalized in terms of changes in the Pt/WO_x boundary line density.⁷⁰ At low deposition times between 20 and 35 s, the Pt island density increases systematically, but the island diameter remains roughly constant. This leads to a systematic increase in Pt/WO_x boundary line density, which enhances the rate of H-spillover and leads to a systematic increase in HOR current (Figure 5b). For Pt deposition times beyond 35 s (40 and 45 s), the Pt islands begin to overlap, which leads to a dramatic decrease in Pt/WO_x line density and a corresponding decline in the rate of H-spillover that further translates into lower HOR current densities. Together, the data indicate that the rate of H-spillover across the Pt/WO_x boundary limits the overall rate of HOR catalysis mediated by the MEPC membrane. To obtain a quantitative analysis of the boundary density, we drew ellipses to estimate the outlines of the Pt particles (Figure S13). By measuring the total perimeters of these ellipses, we obtained a crude estimation of the Pt/WO_x boundary length. By plotting the boundary length versus Pt deposition time, we find that the boundary length first increases with increasing Pt deposition time from 20 to 35 s and then the boundary length decreases for 40 and 45 s Pt deposition times (Figure S14). The results further suggest that varying the Pt deposition time alters the Pt/WO_x boundary density which in turn affects the rate of H-spillover and overall HOR catalysis.

The final step of HOR catalysis of the Pt/WO_x composite electrode involves electron–proton charge separation at the $\text{WO}_x/\text{electrolyte}$ interface. While the known corrosion

instability of WO_x in base restricted our studies to acidic environments,^{71–73} we found that varying the H^+ concentration from 0.1 to 2.0 M did not lead to a simple Nernstian shift of the open-circuit potential or a corresponding shift of the polarization curves to more negative values as the pH was increased. Instead, the lowest H^+ concentration, 0.1 M, displays a slightly decreased slope but a very similar open circuit potential to the curves at higher H^+ concentration (Figure S16). While a complete understanding of the origin of these effects awaits an *in situ* picture of the structure of the $\text{WO}_x/\text{solution}$ interface under polarization, these observations exclude a simple reversible one-electron, one-proton equilibrium with solution defining the potential at the $\text{WO}_x/\text{solution}$ interface. Instead, we postulate that this electron–proton transfer is irreversible at the $\text{WO}_x/\text{solution}$ interface under the conditions of catalysis.

The above analysis allows us to assemble a qualitative model for HOR catalyzed by the Pt/WO_x MEPC membrane (Figure 6). The applied electrochemical potential directly alters the

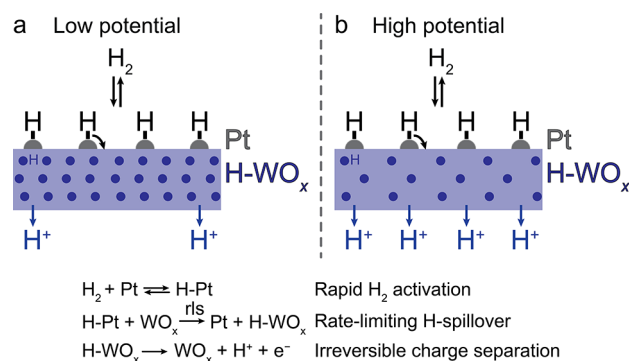


Figure 6. Putative mechanism for HOR catalysis at Pt/WO_x composite electrodes. More positive potentials (b) decrease the H concentration within WO_x relative to low applied potentials (a). We invoke rate limiting H-spillover which is accelerated by a lower H concentration in WO_x .

driving force and thus, the rate of electron–proton charge separation at the solution interface. The increased rate of H extraction from WO_x serves to decrease the H population in the WO_x film. Due to rapid H-diffusion in WO_x , this decrease in H population is rapidly felt at the Pt/WO_x interface. This, in turn, causes an increase in the number of WO_x sites available to accept H from the Pt surface at the Pt/WO_x interface. In this way, the applied potential serves to indirectly augment the rate of H-spillover via variation in the H population of WO_x . At steady state, the rates of charge separation and H-spillover must be equivalent, balanced by an appropriate H population. Thus, we postulate that the correlation between the H population and rate of H-spillover give rise to the observed linear I – V profile. However, we note that the precise slope of the linear I – V profile may also contain contributions from lateral electrical resistances across the WO_x film from the site of charge separation to the radial current collector, as well as the possibility of ionic resistances that arise from a space-charge region that could form at the $\text{WO}_x/\text{solution}$ interface.⁷⁴ Ongoing studies are aimed at tracking the H population *in situ* to build a quantitative model for the kinetic and resistive contributions to the observed HOR polarization behavior on MEPC membranes.

CONCLUSIONS

Here, we establish a method for spatially separating the critical electrocatalytic processes of substrate bond activation and electron–proton charge separation. We show that interposing a mixed electron–proton conducting (MEPC) WO_x membrane between a Pt catalyst and aqueous electrolyte generates a composite electrode for HOR catalysis. In this electrode, the electrochemical driving force for electron–proton charge separation at the oxide/electrolyte interface is translated into a chemical driving force for H_2 activation and H-spillover at the Pt/WO_x interface, enabling overall HOR catalysis. In this way, the MEPC membrane enables electrochemical polarization to be used to drive catalytic reactions at gas/solid interfaces, thereby spatially segregating the critical bond activation and charge separation steps of electrocatalysis.

This spatial segregation endows the Pt/WO_x MEPC electrode with unique electrocatalytic properties that are impossible to achieve with a traditional electrode consisting of the singular interface. Since H_2 activation occurs directly at the gas/Pt interface, we are able to achieve HOR current densities that are 8-fold larger than the diffusion-limited rate of HOR catalysis at a singular Pt/solution interface. Furthermore, since the Pt catalyst surface is not in contact with the electrolyte and the WO_x is exceptionally selective for H-transport, the MEPC electrode displays excellent tolerance to poisons and impurities dissolved in the electrolyte or that crossover from the cathode.

This study also establishes the key factors that control the efficiency of MEPC electrocatalysis. Remarkably, we find that the WO_x membrane supports facile H-diffusion even at room temperature and find that the rate of catalysis is principally controlled by the rate of H-spillover at the Pt/WO_x boundary. These mechanistic insights establish a path toward higher-efficiency MEPCs electrodes by maximizing the Pt/WO_x boundary density. Given the wide diversity of known H-intercalating materials with a wide range of H-affinities, the concept established here provides the basis of segregating bond activation and charge separation processes across a wide range of key energy conversion reactions.

ASSOCIATED CONTENT

Supporting Information

The Supporting Information is available free of charge on the ACS Publications website at DOI: 10.1021/jacs.9b03327.

Complete experimental details, ICP-MS data, and additional cyclic voltammograms, chronoamperograms, SEM images, TEM images, STEM-EDS results, XRD data, and XPS data (PDF)

AUTHOR INFORMATION

Corresponding Author

*yogi@mit.edu

ORCID

Bing Yan: 0000-0001-7874-725X

Alexander Alabugin: 0000-0001-6307-5016

Yogesh Surendranath: 0000-0003-1016-3420

Notes

The authors declare the following competing financial interest(s): B.Y. and Y.S. are inventors on patent application No. 62/717,381 submitted by the Massachusetts Institute of

Technology that covers the mixed electron-proton conducting membranes described in this work.

ACKNOWLEDGMENTS

We thank Fikile Brushett, Shane Ardo, Marcel Schreier, Michael Pegis, Thejas Wesley, Youngmin Yoon, and Corey Kaminsky for helpful discussions. We thank Ling Xie and Ed Macomber for advice on sample fabrication. We thank Jules Gardener for her help with STEM-EDS characterizations. This research was supported by the NSF under award CHE-1454060. XPS, TEM, and XRD characterizations made use of Shared Experimental Facilities supported in part by the MRSEC Program of the National Science Foundation under award DMR-0819762. Support for ICP-MS investigations was provided by a core center grant P30-ES002109 from the National Institute of Environmental Health Sciences, National Institutes of Health. Magnetron sputtering fabrications, SEM and STEM-EDS characterizations were performed at the Center for Nanoscale Systems (CNS), a member of the National Nanotechnology Coordinated Infrastructure Network (NNCI), which is supported by the National Science Foundation under NSF award no. 1541959. CNS is part of Harvard University. Y.S. acknowledges the Sloan Foundation, Research Corporation for Science Advancement (Cottrell Scholar), and the Canadian Institute for Advanced Research (CIFAR Azrieli Global Scholar).

REFERENCES

- (1) McCrory, C. C. L.; Jung, S.; Peters, J. C.; Jaramillo, T. F. Benchmarking Heterogeneous Electrocatalysts for the Oxygen Evolution Reaction. *J. Am. Chem. Soc.* **2013**, *135* (45), 16977–16987.
- (2) Kanan, M. W.; Nocera, D. G. In Situ Formation of an Oxygen-Evolving Catalyst in Neutral Water Containing Phosphate and Co^{2+} . *Science* **2008**, *321* (5892), 1072–1075.
- (3) Friebe, D.; Louie, M. W.; Bajdich, M.; Sanwald, K. E.; Cai, Y.; Wise, A. M.; Cheng, M.-J.; Sokaras, D.; Weng, T.-C.; Alonso-Mori, R.; Davis, R. C.; Bargar, J. R.; Nørskov, J. K.; Nilsson, A.; Bell, A. T. Identification of Highly Active Fe Sites in $(\text{Ni},\text{Fe})\text{OOH}$ for Electrocatalytic Water Splitting. *J. Am. Chem. Soc.* **2015**, *137* (3), 1305–1313.
- (4) Li, Y.; Liang, Y.; Wei, F.; Zhou, J.; Wang, J.; Regier, T.; Gong, M.; Wang, H.; Wu, J. Z.; Dai, H. An Advanced Ni–Fe Layered Double Hydroxide Electrocatalyst for Water Oxidation. *J. Am. Chem. Soc.* **2013**, *135* (23), 8452–8455.
- (5) Jin, K.; Seo, H.; Hayashi, T.; Balamurugan, M.; Jeong, D.; Go, Y. K.; Hong, J. S.; Cho, K. H.; Kakizaki, H.; Bonnet-Mercier, N.; Kim, M. G.; Kim, S. H.; Nakamura, R.; Nam, K. T. Mechanistic Investigation of Water Oxidation Catalyzed by Uniform, Assembled MnO Nanoparticles. *J. Am. Chem. Soc.* **2017**, *139* (6), 2277–2285.
- (6) Strmcnik, D.; Uchimura, M.; Wang, C.; Subbaraman, R.; Danilovic, N.; van der Vliet, D.; Paulikas, A. P.; Stamenkovic, V. R.; Markovic, N. M. Improving the Hydrogen Oxidation Reaction Rate by Promotion of Hydroxyl Adsorption. *Nat. Chem.* **2013**, *5* (4), 300–306.
- (7) Wang, H.; Abruña, H. D. IrPdRu/C as H_2 Oxidation Catalysts for Alkaline Fuel Cells. *J. Am. Chem. Soc.* **2017**, *139* (20), 6807–6810.
- (8) Svedružić, D.; Blackburn, J. L.; Tenent, R. C.; Rocha, J. D. R.; Vinzant, T. B.; Heben, M. J.; King, P. W. High-Performance Hydrogen Production and Oxidation Electrodes with Hydrogenase Supported on Metallic Single-Wall Carbonnanotube Networks. *J. Am. Chem. Soc.* **2011**, *133* (12), 4299–4306.
- (9) Alia, S. M.; Pivovar, B. S.; Yan, Y. Platinum-Coated Copper Nanowires with High Activity for Hydrogen Oxidation Reaction in Base. *J. Am. Chem. Soc.* **2013**, *135* (36), 13473–13478.
- (10) Strmcnik, D.; Escudero-Escribano, M.; Kodama, K.; Stamenkovic, V. R.; Cuesta, A.; Marković, N. M. Enhanced

Electrocatalysis of the Oxygen Reduction Reaction Based on Patterning of Platinum Surfaces with Cyanide. *Nat. Chem.* **2010**, *2* (10), 880–885.

(11) Nesselberger, M.; Ashton, S.; Meier, J. C.; Katsounaros, I.; Mayrhofer, K. J. J.; Arenz, M. The Particle Size Effect on the Oxygen Reduction Reaction Activity of Pt Catalysts: Influence of Electrolyte and Relation to Single Crystal Models. *J. Am. Chem. Soc.* **2011**, *133* (43), 17428–17433.

(12) Liang, H.-W.; Wei, W.; Wu, Z.-S.; Feng, X.; Müllen, K. Mesoporous Metal-Nitrogen-Doped Carbon Electrocatalysts for Highly Efficient Oxygen Reduction Reaction. *J. Am. Chem. Soc.* **2013**, *135* (43), 16002–16005.

(13) Wu, Z.-S.; Yang, S.; Sun, Y.; Parvez, K.; Feng, X.; Müllen, K. 3D Nitrogen-Doped Graphene Aerogel-Supported Fe₃O₄ Nanoparticles as Efficient Electrocatalysts for the Oxygen Reduction Reaction. *J. Am. Chem. Soc.* **2012**, *134* (22), 9082–9085.

(14) Singh, M. R.; Kwon, Y.; Lum, Y.; Ager, J. W.; Bell, A. T. Hydrolysis of Electrolyte Cations Enhances the Electrochemical Reduction of CO₂ over Ag and Cu. *J. Am. Chem. Soc.* **2016**, *138*, 13006–13012.

(15) Wuttig, A.; Yaguchi, M.; Motobayashi, K.; Osawa, M.; Surendranath, Y. Inhibited Proton Transfer Enhances Au-Catalyzed CO₂-to-Fuels Selectivity. *Proc. Natl. Acad. Sci. U. S. A.* **2016**, *113* (32), E4585–E4593.

(16) Amatore, C.; Savéant, J.-M. Mechanism and Kinetic Characteristics of the Electrochemical Reduction of Carbon Dioxide in Media of Low Proton Availability. *J. Am. Chem. Soc.* **1981**, *103* (17), 5021–5023.

(17) Gao, D.; Zhou, H.; Wang, J.; Miao, S.; Yang, F.; Wang, G.; Wang, J.; Bao, X. Size-Dependent Electrocatalytic Reduction of CO₂ over Pd Nanoparticles. *J. Am. Chem. Soc.* **2015**, *137* (13), 4288–4291.

(18) Wilhelm, E.; Wilcock, R. J.; Battino, R. Low Pressure Solubility of Gases in Liquid Water. *Chem. Rev.* **1977**, *77* (2), 219–262.

(19) Gang, X. Hydrogen Oxidation on Gas Diffusion Electrodes for Phosphoric Acid Fuel Cells in the Presence of Carbon Monoxide and Oxygen. *J. Electrochem. Soc.* **1995**, *142* (9), 2890.

(20) Strmcnik, D.; Kodama, K.; van der Vliet, D.; Greeley, J.; Stamenkovic, V. R.; Marković, N. M. The Role of Non-Covalent Interactions in Electrocatalytic Fuel-Cell Reactions on Platinum. *Nat. Chem.* **2009**, *1* (9), 466–472.

(21) Yan, J.-W.; He, D.-W.; Mao, B.-W.; Li, M.-G.; Zhang, X.; Zhong, Y.-X. Resolving Fine Structures of the Electric Double Layer of Electrochemical Interfaces in Ionic Liquids with an AFM Tip Modification Strategy. *J. Am. Chem. Soc.* **2014**, *136* (42), 14682–14685.

(22) Richey, F. W.; Dyatkin, B.; Gogotsi, Y.; Elabd, Y. A. Ion Dynamics in Porous Carbon Electrodes in Supercapacitors Using in Situ Infrared Spectroelectrochemistry. *J. Am. Chem. Soc.* **2013**, *135* (34), 12818–12826.

(23) Stamenkovic, V. R.; Strmcnik, D.; Lopes, P. P.; Markovic, N. M. Energy and Fuels from Electrochemical Interfaces. *Nat. Mater.* **2017**, *16* (1), 57–69.

(24) Costentin, C.; Robert, M.; Savéant, J.-M.; Tatin, A. Efficient and Selective Molecular Catalyst for the CO₂-to-CO Electrochemical Conversion in Water. *Proc. Natl. Acad. Sci. U. S. A.* **2015**, *112* (22), 6882–6886.

(25) Jackson, M. N.; Surendranath, Y. Donor-Dependent Kinetics of Interfacial Proton-Coupled Electron Transfer. *J. Am. Chem. Soc.* **2016**, *138* (9), 3228–3234.

(26) Costentin, C.; Drouet, S.; Robert, M.; Savéant, J.-M. A Local Proton Source Enhances CO₂ Electroreduction to CO by a Molecular Fe Catalyst. *Science* **2012**, *338* (6103), 90–94.

(27) Costentin, C.; Robert, M.; Savéant, J. M. Current Issues in Molecular Catalysis Illustrated by Iron Porphyrins as Catalysts of the CO₂-to-CO Electrochemical Conversion. *Acc. Chem. Res.* **2015**, *48* (12), 2996–3006.

(28) Kwon, Y.; Lai, S. C. S.; Rodriguez, P.; Koper, M. T. M. Electrocatalytic Oxidation of Alcohols on Gold in Alkaline Media:

Base or Gold Catalysis? *J. Am. Chem. Soc.* **2011**, *133* (18), 6914–6917.

(29) Joo, J.; Uchida, T.; Cuesta, A.; Koper, M. T. M.; Osawa, M. Importance of Acid-Base Equilibrium in Electrocatalytic Oxidation of Formic Acid on Platinum. *J. Am. Chem. Soc.* **2013**, *135* (27), 9991–9994.

(30) Wuttig, A.; Surendranath, Y. Impurity Ion Complexation Enhances Carbon Dioxide Reduction Catalysis. *ACS Catal.* **2015**, *5*, 4479–4484.

(31) Trzesniewski, B. J.; Diaz-Morales, O.; Vermaas, D. A.; Longo, A.; Bras, W.; Koper, M. T. M.; Smith, W. A. In Situ Observation of Active Oxygen Species in Fe-Containing Ni-Based Oxygen Evolution Catalysts: The Effect of PH on Electrochemical Activity. *J. Am. Chem. Soc.* **2015**, *137* (48), 15112–15121.

(32) Kang, Y.; Li, M.; Cai, Y.; Cargnello, M.; Diaz, R. E.; Gordon, T. R.; Wieder, N. L.; Adzic, R. R.; Gorte, R. J.; Stach, E. A.; Murray, C. B. Heterogeneous Catalysts Need Not Be so “Heterogeneous”: Monodisperse Pt Nanocrystals by Combining Shape-Controlled Synthesis and Purification by Colloidal Recrystallization. *J. Am. Chem. Soc.* **2013**, *135* (7), 2741–2747.

(33) Sherbo, R. S.; Delima, R. S.; Chiykowski, V. A.; MacLeod, B. P.; Berlinguette, C. P. Complete Electron Economy by Pairing Electrolysis with Hydrogenation. *Nat. Catal.* **2018**, *1* (7), 501–507.

(34) Sherbo, R. S.; Kurimoto, A.; Brown, C. M.; Berlinguette, C. P. Efficient Electrocatalytic Hydrogenation with a Palladium Membrane Reactor. *J. Am. Chem. Soc.* **2019**, *141* (19), 7815–7821.

(35) Devanathan, M. A. V.; Stachurski, Z. The Adsorption and Diffusion of Electrolytic Hydrogen in Palladium. *Proc. R. Soc. Lond. A* **1962**, *270* (1340), 90–102.

(36) Güther, W.; Vielstich, W. Investigation on the Electrocatalytic Dehydrogenation of Cho-Compounds in Acidic Media via a Palladium Membrane. *Electrochim. Acta* **1982**, *27* (7), 811–816.

(37) Norby, T. Solid-State Protonic Conductors: Principles, Properties, Progress and Prospects. *Solid State Ionics* **1999**, *125* (1), 1–11.

(38) Fabregat-Santiago, F.; Barea, E. M.; Bisquert, J.; Mor, G. K.; Shankar, K.; Grimes, C. A. High Carrier Density and Capacitance in TiO₂ Nanotube Arrays Induced by Electrochemical Doping. *J. Am. Chem. Soc.* **2008**, *130* (34), 11312–11316.

(39) Wang, G.; Zhang, L.; Zhang, J. A Review of Electrode Materials for Electrochemical Supercapacitors. *Chem. Soc. Rev.* **2012**, *41*, 797–828.

(40) Hersch, H. N.; Kramer, W. E.; McGee, J. H. Mechanism of Electrochromism in WO₃. *Appl. Phys. Lett.* **1975**, *27* (12), 646–648.

(41) Zeller, H. R.; Beyeler, H. U. Electrochromism and Local Order in Amorphous WO₃. *Appl. Phys.* **1977**, *13* (3), 231–237.

(42) Prins, R. Hydrogen Spillover. Facts and Fiction. *Chem. Rev.* **2012**, *112* (5), 2714–2738.

(43) Srinivas, S. T.; Rao, P. K. Direct Observation of Hydrogen Spillover on Carbon-Supported Platinum and Its Influence on the Hydrogenation of Benzene. *J. Catal.* **1994**, *148* (2), 470–477.

(44) Crandall, R. S.; Wojtowicz, P. J.; Faughnan, B. W. Theory and Measurement of the Change in Chemical Potential of Hydrogen in Amorphous H_xWO₃ as a Function of the Stoichiometric Parameter x. *Solid State Commun.* **1976**, *18* (11–12), 1409–1411.

(45) Zheng, H.; Ou, J. Z.; Strano, M. S.; Kaner, R. B.; Mitchell, A.; Kalantar-Zadeh, K. Nanostructured Tungsten Oxide - Properties, Synthesis, and Applications. *Adv. Funct. Mater.* **2011**, *21* (12), 2175–2196.

(46) LeGore, L. J.; Lad, R. J.; Moulzolf, S. C.; Vetelino, J. F.; Frederick, B. G.; Kenik, E. A. Defects and Morphology of Tungsten Trioxide Thin Films. *Thin Solid Films* **2002**, *406* (1–2), 79–86.

(47) Vemuri, R. S.; Engelhard, M. H.; Ramana, C. V. Correlation between Surface Chemistry, Density, and Band Gap in Nanocrystalline WO₃ Thin Films. *ACS Appl. Mater. Interfaces* **2012**, *4* (3), 1371–1377.

(48) Fleisch, T. H.; Mains, G. J. An XPS Study of the UV Reduction and Photochromism of MoO₃ and WO₃. *J. Chem. Phys.* **1982**, *76* (2), 780–786.

- (49) Paparazzo, E. On the Interpretation of XPS Spectra of Metal (Pt, Pt-Sn) Nanoparticle/Graphene Systems. *Carbon* **2013**, *63*, 578–581.
- (50) Kocha, S. S.; Deliang Yang, J.; Yi, J. S. Characterization of Gas Crossover and Its Implications in PEM Fuel Cells. *AIChE J.* **2006**, *52* (5), 1916–1925.
- (51) Fenton, J. M.; Rodgers, M. P.; Slattey, D. K.; Huang, X.; Mittal, V. O.; Bonville, L. J.; Kunz, H. R. Membrane Degradation Mechanisms and Accelerated Durability Testing of Proton Exchange Membrane Fuel Cells. In *ECS Transactions*; ECS, 2009; Vol. 25, pp 233–247.
- (52) Allian, A. D.; Takanabe, K.; Fujidala, K. L.; Hao, X.; Truex, T. J.; Cai, J.; Buda, C.; Neurock, M.; Iglesia, E. Chemisorption of CO and Mechanism of CO Oxidation on Supported Platinum Nanoclusters. *J. Am. Chem. Soc.* **2011**, *133* (12), 4498–4517.
- (53) Moses-Debusk, M.; Yoon, M.; Allard, L. F.; Mullins, D. R.; Wu, Z.; Yang, X.; Veith, G.; Stocks, G. M.; Narula, C. K. CO Oxidation on Supported Single Pt Atoms: Experimental and Ab Initio Density Functional Studies of CO Interaction with Pt Atom on θ -Al₂O₃(010) Surface. *J. Am. Chem. Soc.* **2013**, *135* (34), 12634–12645.
- (54) Liu, J.; Lucci, F. R.; Yang, M.; Lee, S.; Marcinkowski, M. D.; Therrien, A. J.; Williams, C. T.; Sykes, E. C. H.; Flytzani-Stephanopoulos, M. Tackling CO Poisoning with Single-Atom Alloy Catalysts. *J. Am. Chem. Soc.* **2016**, *138*, 6396–6399.
- (55) Markovic, N.; Ross, P. N. Effect of Anions on the Underpotential Deposition of Cu on KPt(111) and Pt(100) Surfaces. *Langmuir* **1993**, *9* (2), 580–590.
- (56) Phair, J. W.; Badwal, S. P. S. Review of Proton Conductors for Hydrogen Separation. *Ionics* **2006**, *12*, 103–115.
- (57) Lin, H.; Zhou, F.; Liu, C.-P.; Ozoliņš, V. Non-Grotthuss Proton Diffusion Mechanism in Tungsten Oxide Dihydrate from First-Principles Calculations. *J. Mater. Chem. A* **2014**, *2* (31), 12280–12288.
- (58) Vannice, M. A.; Boudart, M.; Fripiat, J. J. Mobility of Hydrogen in Hydrogen Tungsten Bronze. *J. Catal.* **1970**, *17* (3), 359–365.
- (59) Zhang, H.; Wan, Q.; Wan, C.; Wu, G.; Zhu, L. Tungsten Oxide Proton Conducting Films for Low-Voltage Transparent Oxide-Based Thin-Film Transistors. *Appl. Phys. Lett.* **2013**, *102* (5), 052905–1–4.
- (60) Sermon, P. A.; Bond, G. C. Studies of Hydrogen Spillover. Part 1.-Study of the Rate, Extent and Products of Hydrogen Spillover from Platinum to the Trioxides of Tungsten and Molybdenum. *J. Chem. Soc., Faraday Trans. 1* **1976**, *72* (0), 730–744.
- (61) Levy, R. B.; Boudart, M. The Kinetics and Mechanism of Spillover. *J. Catal.* **1974**, *32* (2), 304–314.
- (62) Nishimura, K. Proton Mobility in H_xWO₃ measured by Proton Magnetic Resonance. *Solid State Commun.* **1976**, *20* (5), 523–524.
- (63) Dickens, P. G.; Murphy, D. J.; Halstead, T. K. Pulsed NMR Study of Proton Mobility in a Hydrogen Tungsten Bronze. *J. Solid State Chem.* **1973**, *6* (3), 370–373.
- (64) Monk, P. M. S. Charge Movement through Electrochromic Thin-Film Tungsten Trioxide. *Crit. Rev. Solid State Mater. Sci.* **1999**, *24* (3), 193–226.
- (65) Christmann, K.; Ertl, G.; Pignet, T. Adsorption of Hydrogen on a Pt(111) Surface. *Surf. Sci.* **1976**, *54* (2), 365–392.
- (66) Christmann, K.; Ertl, G. Interaction of Hydrogen with Pt(111): The Role of Atomic Steps. *Surf. Sci.* **1976**, *60* (2), 365–384.
- (67) Poelsema, B.; Lenz, K.; Comsa, G. The Dissociative Adsorption of Hydrogen on Defect-free Pt(111). *J. Phys.: Condens. Matter* **2010**, *22* (30), 304006–304015.
- (68) Sermon, P. A.; Bond, G. C. Studies of Hydrogen Spillover: Part 4. - Factors Affecting Hydrogen Spillover and Its Reversal. *J. Chem. Soc., Faraday Trans. 1* **1980**, *76* (0), 889–900.
- (69) Luntz, A. C.; Brown, J. K.; Williams, M. D. Molecular Beam Studies of H₂ and D₂ Dissociative Chemisorption on Pt(111). *J. Chem. Phys.* **1990**, *93* (7), 5240–5246.
- (70) Horprathum, M.; Srichaiyaperk, T.; Samransuksamer, B.; Wisitsoraat, A.; Eiamchai, P.; Limwichean, S.; Chananonwathorn, C.; Aiempnanakit, K.; Nuntawong, N.; Patthanasettakul, V.; Oros, C.; Porntheeraphat, S.; Songsirittithigul, P.; Nakajima, H.; Tuantranont, A.; Chindaudom, P. Ultrasensitive Hydrogen Sensor Based on Pt-Decorated WO₃ Nanorods Prepared by Glancing-Angle DC Magnetron Sputtering. *ACS Appl. Mater. Interfaces* **2014**, *6* (24), 22051–22060.
- (71) Takeno, N. Atlas of Eh-PH Diagrams Intercomparison of Thermodynamic Databases. *Geol. Surv. Japan* **2005**, No. 419, 272–273.
- (72) Shah Idil, A.; Donaldson, N. The Use of Tungsten as a Chronically Implanted Material. *J. Neural Eng.* **2018**, *15* (2), 021006–021018.
- (73) Zhu, T.; Chong, M. N.; Chan, E. S. Nanostructured Tungsten Trioxide Thin Films Synthesized for Photoelectrocatalytic Water Oxidation: A Review. *ChemSusChem* **2014**, *7* (11), 2974–2997.
- (74) Faughnan, B. W.; Crandall, R. S.; Lampert, M. A. Model for the Bleaching of WO₃ Electrochromic Films by an Electric Field. *Appl. Phys. Lett.* **1975**, *27* (5), 275–277.